INVISCID/VISCOUS HYPERSONIC FLOW IN CONFINED DUCTS AND AROUND OF IMMERSED BODIES CONSIDERING ANISOTROPIC SHOCK CAPTURING AND ADAPTIVE MESH REFINEMENT TECHNIQUES

Rodrigo R. PAZ, Norberto M. NIGRO and Mario A. STORTI.
Centro Internacional de Métodos Computacionales en Ingeniería (CIMEC)
CONICET - INTEC - U.N.L.
Güemes 3450, (3000) Santa Fe, Argentina
e-mail: `rodrigop@intec.unl.edu.ar`, `http://www.cimec.org.ar/`

Key Words: hypersonic flow, domain decomposition technique, parallel computing, shock capturing, adaptive refinement.

Abstract.

In this paper, we present a numerical study of the viscous/inviscid hypersonic flows in confined ducts and around of immersed bodies. Nowadays the flow at high Mach numbers and its interaction with deformable structures is considered a 'challenge' in the context of numerical methods.

In hypersonic flow problems the non-linearities become high and any difficulty in the convergence of the linear system may influence the nonlinear convergence and finally make the solution to blow up. Then, global iteration result in a non suitable scheme (high cpu and memory demands for preconditioned GMRes method, for instance) for this step. A new preconditioner for domain decomposition methods (see References[1,2,3]) is used in order to obtain physical solutions and to accelerate the convergence to a low tolerance in residuals.

In order to diminish the solution error near physical discontinuities (e.g. contact layers, shock waves) or expansion shocks an adaptive mesh refinement technique is used. Besides, an anisotropic shock capturing operator is added to the Galerkin/SUPG formulation.

Also in this work, we present results of a new methodology for imposing absorbing boundary conditions for general advective-diffusive system of equations (e.g., the compressible Navier-Stokes equations). Basically, two types of local absorbing boundary conditions (b.c.) are considered, i.e. the linear absorbent b.c., based on the Jacobian of the flux function, assuming small perturbations about a reference value, and the general non-linear absorbent b.c. based on the Riemann invariants of the problem (see Reference[4] for a more detailed description).

1 INTRODUCTION.

Accurate prediction of laminar-to-turbulent transition in boundary-layer flows is a key in the aero-thermodynamic design and optimization of many aeronautical/aerospace configurations, such as high-lift systems, quiet and ultra-efficient supersonic aircraft, reentry bodies, and hypersonic air-intakes. The prediction of mechanical and thermal loads on the surfaces of hypersonic vehicles is essential for the design of their aerodynamic shape and thermal shields. The control surfaces (such as elevators and flaps) are immersed in the flow field of the vehicle and are dominated by shock wave/boundary layer interactions that can cause extended separations, laminar/turbulence transition, intense localized heating and chemical reactions that feed from its production and cause the change of the fluid properties. These interactions produces an increase of drag and lift forces, that generate a variation of the hinge moment and change the aerodynamic efficiency (generally, a loss) of the control surfaces. Experimental and theoretical studies dealing with the *shock wave/boundary layer* interaction over compression ramps were conducted in the past half-century for both laminar and turbulent conditions and for low enthalpy hypersonic flows. Extensive reviews describing the physical features of a shock wave/boundary layer interaction in that regime can be found in the works of Chapman *et al.*,[5] Délery[6] and the references therein.

Experimental studies were conducted by Holden[7] (laminar and turbulent regimes) in order to study the shock wave/boundary layer interactions from supersonic through hypersonic regime. Holden established that "*upstream influence decreases with Mach number and increases with ramp angle and, and it is affected also by the Reynolds number (weakly in a fully turbulent regime), while bluntness reduces pressure and thermal loads since the interaction occurs in a locally supersonic regime*". Later, it was shown experimentally that the upstream influence and separation length (a measure of the intensity of a shock wave/boundary layer interaction) increase with ramp angle (for fixed Mach and Reynolds numbers) and that decrease with Mach number (for fixed ramp angle and Reynolds).

On the other hand, the treatment of the equations that governs the inviscid flow at supersonic Mach numbers with numerical techniques has received a wealth of attention in finite differences and finite volumes techniques since the pioneering work of Sod,[8] Moretti[9] and Hirsch *et al.*[10] in late seventies and middle eighties; and the articles of Grasso and Marini[11,12] in nineties.

One of the most challenging tasks in numerical simulations of compressible viscous flows is the approximation of thin boundary layers which develop in a gas along walls of a solid obstacle. Recent articles of Jiang *et al.*[13] and Zhong and Tatineni[14] studied the instability and transition (laminar to turbulent) of hypersonic boundary layers by means of Direct Numerical Simulations (DNS, via a high order finite difference method) and Parabolized Stability Equations (PSE) techniques.

Rachowicz, in Reference,[15] introduced an application of the finite element method with significantly stretched elements (in an adaptive process as a result of selective directional subsecting of elements) to solve compressible Navier-Stokes equations. Rachowicz used an iterative solver (i.e, the GMRes algorithm with a domain decomposition Schwarz-type preconditioner

similar to block-Jacobi preconditioner) with the convergence characteristics independent of the aspect ratio of elements.

In this work, we present a model to study the flow (viscous/inviscid) at high Mach numbers around bodies by means of a parallel stabilized finite element method considering an anisotropic shock-capturing operator and a *h*-adaptive refinement technique. Also, a new preconditioner for domain decomposition method (see References[1,2,3] is used in order to obtain physical solutions and to accelerate the convergence to a low tolerance in residuals when the condition of the (inner) linear system grows substantially due to high gradients in refinement and the high non-linearity of the physical problem. A new local non-reflecting boundary condition, based on the Jacobian of the flux functions, is used in order to avoid wave reflections at the intersections of subsonic regions and fictitious walls. The approach used here do not consider chemical reactions.

2 PHYSICAL MODEL.

We focus this work in the solution of compressible Navier-Stokes equations with the SUPG/SC (*"Streamline Upwind Petrov-Galerkin/Shock Capturing*) method proposed by Brooks *et al.* in Reference[16] and by Aliabady *et al.* in Reference[17]

2.1 The compressible Navier-Stokes equations.

The differential form of the conservation equations of mass, momentum and total energy that governs the dynamics of compressible and viscous fluid flow may be written in a compact intrinsic (vector) form as (Einstein summation convention is assumed, $i, j = 1, 2, 3$):

$$\frac{\partial \mathbf{U}}{\partial t} + \frac{\partial (\mathcal{F}^a)_i}{\partial x_i} = \frac{\partial (\mathcal{F}^d)_i}{\partial x_i} + \mathcal{G} \quad \text{in } \Omega \times (0, t_+] \tag{1}$$

where Ω is the model domain with boundary Γ. $\mathbf{U} = (\rho, \rho\mathbf{u}, \rho e)^t$ is the unknown state vector expressed in conservative variables as above, e represents the specific total energy, $\mathcal{F}^a$ accounts for the (vector) advective fluxes, $\mathcal{F}^d$ for the (vector) diffusive fluxes and $\mathcal{G}$ is used for the external source terms (i.e $\mathcal{G} = (0, \rho\mathbf{f_e}, W_f + q_H)$, $W_f = \rho\mathbf{f_e} \cdot \mathbf{u}$ is the work done by the external forces $\mathbf{f_e}$ and $\mathbf{n}$ represents the boundary unit normal vector). Also, initial and boundary condition must be added (see[10]). In this article, we treat the so called *absorbent* boundary conditions. The integral conservation form is

$$\frac{\partial}{\partial t} \int_\Omega \begin{pmatrix} \rho \\ \rho\mathbf{u} \\ \rho e \end{pmatrix} d\Omega + \oint_\Gamma \begin{pmatrix} \rho\mathbf{u} \\ \rho\mathbf{u} \otimes \mathbf{u} + p\bar{\bar{I}} - \bar{\bar{\tau}} \\ \rho\mathbf{u}H - \bar{\bar{\tau}} \cdot \mathbf{u} - k\nabla T \end{pmatrix} \cdot \mathbf{n}d\Gamma = \int_\Omega \begin{pmatrix} 0 \\ \rho\mathbf{f_e} \\ W_f + q_H \end{pmatrix} d\Omega \tag{2}$$

In (2), $\mathcal{H}$ is the total specific enthalpy defined in terms of the specific internal energy Ξ and the specific kinetic energy as $\mathcal{H} = h + \frac{1}{2}|\mathbf{u}|^2$ and $h = \Xi + p/\rho$, respectively. The above

mentioned advective and diffusive fluxes are defined as:

$$
\mathcal{F}^a = \begin{pmatrix} \rho u_i \\ \rho u_1 u_i + \delta_{i1} p \\ \rho u_2 u_i + \delta_{i2} p \\ \rho u_3 u_i + \delta_{i3} p \\ (\rho e + p) u_i \end{pmatrix}, \quad \mathcal{F}^d = \begin{pmatrix} 0 \\ \tau_{i1} \\ \tau_{i2} \\ \tau_{i3} \\ \tau_{ik} u_k - q_i \end{pmatrix}.
\tag{3}
$$

Here δ_{ij} is the Kronecker isotropic tensor of rank 2 (also denoted as $\mathbf{I}$), q_i are the components of the heat flux vector, and τ_{ij} are the components of the Newtonian viscous stress tensor: $\bar{\bar{\tau}} = 2\mu\epsilon(\mathbf{u}) - 2/3\mu(\nabla \cdot \mathbf{u})\mathbf{I}$. The strain rate tensor ϵ is $\epsilon(\mathbf{u}) = \frac{1}{2}(\partial_j u_i + \partial_i u_j)$. q_i is the heat flux defined according to the Fourier law assumptions as: $q_i = -\kappa\nabla T$ with κ the thermal conductivity and T the temperature. The coefficients of viscosity and thermal conductivity are assumed be given by the Sutherland formula (i.e, the gas is considered in a *standard atmosphere*),

$$
\mu = \mu_0 \left(\frac{T}{T_0}\right)^{3/2} \frac{T_0 + 110}{T + 110} \quad \kappa = \frac{\gamma R \mu}{(\gamma - 1) Pr},
\tag{4}
$$

where μ_0 is the viscosity at the reference temperature T_0 and Pr is the Prandtl number (i.e., $Pr = \nu/\iota$, ι is the thermal diffusivity coefficient).

The physical model is closed by the definition of the constitutive law for the specific internal energy in terms of the thermodynamic state and some state equation for the thermodynamic variables, normally an ideal gas law is adopted, then $\rho e = \frac{p}{\gamma - 1} + \frac{1}{2}\rho\|\mathbf{u}\|^2$ and $p = \rho R T$; where $R = (\gamma - 1) C_v$ is the particular gas constant and $\gamma = \frac{C_p}{C_v}$ is the ratio of the specific heat at constant pressure relative to that at constant volume. Alternatively equation (2) can be written in the quasi-linear form:

$$
\frac{\partial \mathbf{U}}{\partial t} + \mathbf{A_i} \frac{\partial \mathbf{U}}{\partial x_i} = \frac{\partial}{\partial x_i}\left(\mathbf{K}_{ij} \frac{\partial \mathbf{U}}{\partial x_j}\right) + \mathcal{G}
\tag{5}
$$

where we have made the assumption that the flux vectors are only function of the state variables, i.e. $\mathcal{F}^a = \mathcal{F}^a(\mathbf{U})$ and $\mathcal{F}^d = \mathcal{F}^d(\mathbf{U})$. Then we can write the divergence of the flux vector functions as $\frac{\partial \mathcal{F}^a}{\partial x_i} = \frac{\partial \mathcal{F}^a}{\partial \mathbf{U}} \frac{\partial \mathbf{U}}{\partial x_i} = \mathbf{A}_i \frac{\partial \mathbf{U}}{\partial x_i}$ and $\frac{\partial \mathcal{F}^d}{\partial x_i} = \frac{\partial \mathcal{F}^d}{\partial \mathbf{U}} \frac{\partial \mathbf{U}}{\partial x_i} = \mathbf{K}_{ij} \frac{\partial \mathbf{U}}{\partial x_i}$.

2.2 Inviscid approximation.

In some particular cases, when inertial forces are predominant over viscous effects and no heat conduction is considered, the fluid motion is described by the Euler equations and they are obtained from the Navier-Stokes equations neglecting all shear stresses and heat conduction terms. This is a valid approximation for flows at high Reynolds numbers ($Re = \|\mathbf{u}\|L/\nu$, L is a characteristic length scale and ν is the kinematic viscosity). The use of this approach changes

the mathematical behavior of the set of equations. The set of differential equations becomes first order and hyperbolic. The boundary conditions must be reformulated and the solution can accept discontinuous variables. The imposition of non-reflecting boundary conditions will be treated further.

2.3 Variational formulation.

Now we present the variational formulation of the compressible Navier-Stokes equations using SUPG finite elements method and the shock capturing operator. Consider a finite element discretization of the Ω into sub-domains $\Omega^e, e = 1, 2, \ldots, n_{\mathrm{el}}$. Based on this discretization we define the finite element function spaces for the trial solutions and for the weighting functions as $\mathcal{V}^h$ and $\mathcal{S}^h$ respectively. These function spaces are selected, by taking the Dirichlet boundary conditions into account, as subsets of $[\mathbf{H}^{1h}(\Omega)]^{n_{\mathrm{d.o.f.}}}$, where $\mathbf{H}^{1h}(\Omega)$ is the finite dimensional Sobolev functional space over Ω, and $n_{\mathrm{d.o.f.}} = n_{\mathrm{sd}} + 2$ is the number of degrees of freedom in the continuum problem and n_{sd} is the space dimension.

The stabilized finite element formulation of the quasi-linear form of (1) is written as follows: find $\mathbf{U}^h \in \mathcal{S}^h$ such that $\forall\, \mathbf{W}^h \in \mathcal{V}^h$

$$
\begin{aligned}
&\int_\Omega \mathbf{W}^h \cdot \left(\frac{\partial \mathbf{U}^h}{\partial t} + \frac{\partial \mathbf{F}_a^h}{\partial x_i} \right) d\Omega = \int_\Omega \mathbf{W}^h \cdot \left(\frac{\partial \mathbf{F}_d^h}{\partial x_i} + \mathcal{G} \right) d\Omega \\
&\int_\Omega \mathbf{W}^h \cdot \left(\frac{\partial \mathbf{U}^h}{\partial t} + \mathbf{A}_i^h \frac{\partial \mathbf{U}^h}{\partial x_i} - \mathcal{G} \right) d\Omega + \int_\Omega \frac{\partial \mathbf{W}^h}{\partial x_i} \cdot \mathbf{K}_{ij}^h \frac{\partial \mathbf{U}^h}{\partial x_j} d\Omega - \int_{\Gamma_h} \mathbf{W}^h \cdot H^h d\Gamma + \\
&+ \sum_{e=1}^{n_{\mathrm{el}}} \int_{\Omega^e} \tau (\mathbf{A}_k^h)^T \frac{\partial \mathbf{W}^h}{\partial x_k} \cdot \left\{ \frac{\partial \mathbf{U}^h}{\partial t} + \mathbf{A}_i^h \frac{\partial \mathbf{U}^h}{\partial x_i} - \frac{\partial}{\partial x_i} \left(\mathbf{K}_{ij}^h \frac{\partial \mathbf{U}^h}{\partial x_j} \right) - \mathcal{G} \right\} d\Omega + \\
&+ \sum_{e=1}^{n_{\mathrm{el}}} \int_{\Omega^e} \delta_{shc} \frac{\partial \mathbf{W}^h}{\partial x_i} \cdot \frac{\partial \mathbf{U}^h}{\partial x_i} d\Omega = \mathbf{0}
\end{aligned}
\tag{6}
$$

where

$$
\begin{aligned}
\mathcal{S}^h &= \{ \mathbf{U}^h | \mathbf{U}^h \in [\mathbf{H}^{1h}(\Omega)]^{n_{\mathrm{d.o.f.}}}, \mathbf{U}^h|_{\Omega^e} \in [P^1(\Omega^e)]^{n_{\mathrm{d.o.f.}}}, \mathbf{U}^h = \mathbf{g} \text{ on} \Gamma_g \} \\
\mathcal{V}^h &= \{ \mathbf{W}^h | \mathbf{W}^h \in [\mathbf{H}^{1h}(\Omega)]^{n_{\mathrm{d.o.f.}}}, \mathbf{W}^h|_{\Omega^e} \in [P^1(\Omega^e)]^{n_{\mathrm{d.o.f.}}}, \mathbf{W}^h = \mathbf{0} \text{ on} \partial\Omega_g \}
\end{aligned}
\tag{7}
$$

where matrices $\mathbf{A}_i$ and $\mathbf{K}_{ij}$ are defined in section §2.1.

The first three terms inside the first two integrals in the variational formulation (6) constitute the Galerkin formulation of the problem, the third integral accounts for the Neumann boundary conditions. The first series of element level integrals in (6) are the SUPG stabilization terms added to prevent spatial oscillations in the advection-dominated range. The second series of element level integrals in (6) are the shock capturing terms added to assure the stability at high Mach and Reynolds number flows, specially to suppress spurious overshoot and undershoot effects in the vicinity of discontinuities.

Various options for calculating the stabilization parameters and defining the shock capturing terms in the context of the SUPG formulation were introduced in Reference.[18] In this section we describe some of these options. The first one is the standard SUPG intrinsic time tensor τ introduced by Aliabadi and Tezduyar in Reference.[17] In this case this matrix is defined as $\tau = \max[\mathbf{0}, \tau_a - \tau_d - \tau_\delta]$, with each τ_x taking into account the advective and diffusive effects and also avoiding the duplication of the shock capturing operator and the streamline upwind operator. These matrices are defined as:

$$\tau_a = \frac{h}{2(c + |\mathbf{u}|)}\mathbf{I}, \quad \tau_d = \frac{\sum_{j=1}^{n_{\text{sd}}} \beta_j^2 \operatorname{diag}(\mathbf{K}_{jj})}{(c + |\mathbf{u}|)^2}\mathbf{I}, \quad \tau_\delta = \frac{\delta_{shc}}{(c + |\mathbf{u}|)^2}\mathbf{I}, \tag{8}$$

where c is the acoustic speed, $h = 2\left(\sum_{a=1}^{n_{\text{en}}} |\mathbf{u} \cdot \nabla N_a|\right)^{-1}$ is the element size computed here as the element length in the direction of the streamline using for its definition the multi-lineal trial function N_a. δ_{shc} is the shock capturing parameter defined in the next paragraph. The τ matrix computation is already an open problem because it is not possible to diagonalize the system of equations. It follows some heuristics arguments based on the maximum value of the set of eigenvalues of the advective jacobian matrices for the characteristic velocity, some measure of the element size that may not be very well justified but is equivalent to any other element size and some mechanism able to remove stabilization when physical diffusion is present.

The design of the shock capturing operator is also an open problem. Here two version, one isotropic and other anisotropic are presented, both of them proposed by Tezduyar *et al.*[19] First a unit vector oriented with the density gradient is defined as $\mathbf{j} = nabla\rho^h/|\nabla\rho^h|$ and a characteristic length as $h_{JGN} = 2\left(\sum_{a=1}^{n_{\text{en}}} |\mathbf{j} \cdot \nabla N_a|\right)^{-1}$, where N_a the finite element shape function corresponding to a node. The above cited isotropic shock capturing factor included in (6) is then defined as:

$$\delta_{shc} = \frac{h_{JGN}}{2} u_{char} \left(\frac{|\nabla\rho^h| h_{JGN}}{\rho_{ref}}\right)^\beta \tag{9}$$

where $u_{char} = |\mathbf{u}| + c$ is the characteristic velocity defined in this work as the addition of the flow velocity magnitude and the acoustic speed. ρ_{ref} is the gaussian point interpolated density and β parameter may be taken as 1 or 2 according to the sharpness of the discontinuity to be captured as suggested in Reference.[19] However in this work only $\beta = 1$ was successfully used.

The anisotropic version of the shock capturing term in (6) is changed as follows:

$$\sum_{e=1}^{n_{\text{el}}} \int_{\Omega^e} \frac{\partial \mathbf{W}^h}{\partial x_i} \mathbf{j}_i \delta_{shc} \mathbf{j}_k \frac{\partial \mathbf{U}^h}{\partial x_k} d\Omega. \tag{10}$$

The anisotropic shock capturing term had shown a good behavior, however for some applications, both terms may be needed, the isotropic one weighted by a factor close to 0.1 or lower.

2.4 Adaptive refinement.

Here the adaptive refinement strategy is briefly presented for clarity reasons. Further details about the implementation of this technique in PETSc-FEM are included in Reference.[20] The adaptive refinement criterion adopted here is commonly called *homogeneous refinement*, i.e. there are only one type of elements in the whole mesh, triangles or quadrilaterals in 2D and tetrahedra or hexahedra in 3D. For this case it is commonly allowed the existence of irregular nodes, nodes that only exists for only one of the two meshes in contact. In this strategy only one irregular node at the interface between two different refinement levels are allowed with its solution constrained to be a linear combination of the two father nodes at the refined edge. The error indicator marks each one of the elements to be refined at the end of the current computation. The definition of the error indicator depends on the problem at hand and it is not rigorously treated in this work. Once the error indicator finishes its job those elements marked are divided in $2^{n_{sd}}$ elements. The element edges are firstly divided in two, then their associated faces are divided in four and finally for 3D problems the corresponding volume is built with the refined faces. For tetrahedra an special situation is found, this subdivision generates four tetrahedral that are similar to the father one, and an internal octahedron. The octahedron is divided into two pyramids of four faces according to the length or the internal diagonals. Finally each pyramid is divided into two tetrahedras. Once the new mesh is generated, the irregular nodes are identified, the new boundary conditions are added and the current state is linearly interpolated in the new mesh. This strategy is one of several others existing in the literature, having some interesting advantages, among them one associated with the refined mesh quality. For quadrilaterals, triangles and hexahedras is trivial to show that the quality keeps constant. For tetrahedras, it is possible to show that the quality keeps almost constant, with a final quality proportional to the original one with a factor of order one.

2.5 Non-reflecting boundary conditions.

It is often required in gas dynamics, or generally, in CFD computations, that the computational domain used in a flow simulation represent only a subdomain of a larger physical domain. To obtain a numerical solution that closely resembles the physical flow field in this subdomain, ideally the condition at computational boundary should be specified using the physical flow conditions there. Unfortunately, these conditions generally are not known without first solving the larger physical flow field.

It is well-known that non-reflecting boundary conditions (NRBCs) play an important role in fluid flow computations. The need for artificial boundary conditions arises when the domain of the problem is unbounded and extends to infinity. In order to treat the problem numerically, a domain of finite size is required and artificial boundaries are imposed. At these artificial boundaries, NRBCs are sought for to minimize their influences on the flow. A spurious reflection resulting from an inappropriate numerical boundary condition will contaminate the flow field and may entirely spoil the flow computation. For the problems considered in this article, we use local conditions that are similar to the (absorbent) conditions described in Reference[21] and

adapted for problems arising in gas dynamics. The basic idea is to handle the incoming Riemann invariants of the problem from fictitious walls (i.e., they may vanish at computational boundaries). Also, a novel set of dynamical absorbent boundary conditions proposed in Reference[4] are considered.

3 NUMERICAL TESTS.

Trough these test we use a linear system solver (i.e., for the inner most loop) based on domain decomposition techniques that we called IISD+ISP (*"Interface Iterative-Subdomain Direct, with added "Interface Strip Preconditioner"*). This method have shown a high performance (i.e., CPU time and memory requirements, as well as accurate solutions) in a wide range of problems arising in CFD in comparison with other classical solvers and techniques. Moreover, some classical methods have failed to achieve a physical solution, see References[1,2,3] for more datails on this subject. Implementation details of the solver and models are available on the net at `http://www.cimec.org.ar/petscfem`.[22]

3.1 The hypersonic flow over a flat plate test (test conducted in a sequential environment).

In this section the hypersonic flow around a flat plate is analyzed, being a typical flow problem where the nonlinearities are so high that any difficulty in the convergence of the linear system may influence the nonlinear convergence and finally make the solution to blow up. This problem, deeply documented by Carter in Reference,[23] show a strong interaction between the boundary layer and the shock wave and also a discontinuity introduced at the flat plate leading edge where the flow has to stagnate from a very high free stream velocity. Both are sources of numerical drawbacks making this test a very challenge problem. Figure (1) shows the problem definition with a sketch of the physical structures present in the flow field and the boundary condition applied to it.

For solving this problem a compressible laminar Navier-Stokes flow solver was used with a constant viscosity for a Reynolds number of 10^4 based on the flat plate length and the free stream state. The Mach number was chosen as 5. This problem was successfully solved using IISD+ISP solver but it was not possible to obtain a solution with a preconditioned global GMRes solver, using in both cases a Krylov subspace dimension of 200. In this last case after some time steps the solution began to present a poor resolution of the strong shock wave and finally the solution crashed. Figure (2) shows the skin friction coefficient and the Stanton number against theoretical predictions based on analytical solutions of an approximate theory called *Eckert reference enthalpy method*.[24] These results show an acceptable behavior of the numerical results relative to the analytical predictions. The Stanton number is defined as
$\text{St} = \frac{q_{\text{wall}}}{\rho_\infty U_\infty C_p |T_{\text{wall}} - T_\infty^0|}$.

The mesh used was composed by 24150 quadrangular elements and 24462 nodes. In order to capture the high thermal and flow gradients the normal spacing close to the flat plate was chosen about 4×10^{-6}. This kind of examples is for cases where the computational resources are limited

free stream conditions

$\mathbf{u} = u_\infty$
$\mathbf{T} = T_\infty$
$\mathbf{p} = p_\infty$

M_∞

y/L

shock wave

downstream conditions: unknown

boundary layer edge

wall conditions: u=0, T= T_w or $\frac{\partial T}{\partial y}$ =0

p_w **unknown**

x/L
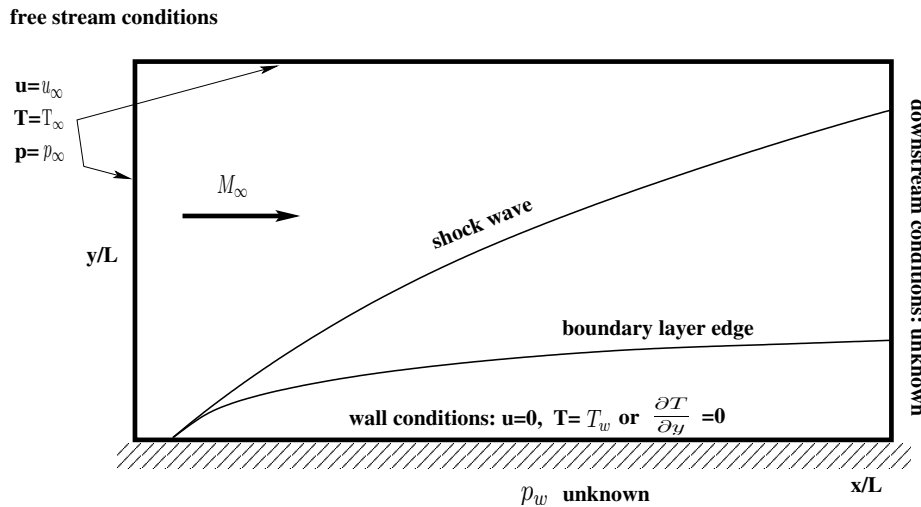
Figure 1: Problem definition.

to single processor architectures and it is not possible to get a solution using preconditioned Global GMRes iteration. Also in such case IISD+ISP does not show any difficulties to get an accurate solution.

3.2 Inviscid hypersonic ramp at Mach=10.

The computational domain for the test case in inviscid configuration is very simple. The angle of the ramp is 15°. For a specific angle of the ramp, two angles of shock wave are solution of the equation. According to the theory of stability, it can be shown that the shock wave corresponding to the highest angle is unstable and it will disappear and that the shock wave corresponding to the lowest angle is stable. This means that if we increase the angle of the ramp up to the limit angle defining the maximum of angle of the shock wave, the shock wave will not be attached to the corner of the ramp anymore and will be positioned before the corner. For a detached shock, the structure is more complex. The characteristics of the flow are that the shock wave is normal to the flat plate before the corner of the ramp and the shape of the shock wave is not linear anymore. The shock wave tends asymptotically to an oblique line far away from the wall. The angle of this line is equal to $\sin^{-1}(1/M_\infty)$. Also, a restricted subsonic region is located just after the shock wave near the corner of the ramp and there is a stagnation point at the corner of the ramp.

In order to conserve attached shock at the corner of the compression ramp, the Mach number at inlet will be chosen equal to 10. The complete characteristics of the inflow are: inlet pressure $p_\infty = 10^5 \mathrm{Pa}$; gas constant $R = 287 \mathrm{J}/(\mathrm{kgK})$; gas specific heat ratio $\gamma = 1.4$ and inlet temperature $T_\infty = 300\mathrm{K}$. With these values the inlet speed of sound is $c = 347.2\mathrm{m/sec}$. As initial flow field, we will consider a uniform flow along x-direction with $M = 10$; $p = 10^5 \mathrm{Pa}$ and $T = 300\mathrm{K}$. The time step was set to 0.01 secs. We consider for this problems the absorbent boundary conditions based on the Riemann invariants of the flux functions. We remark that the

Skin friction

(a) Skin friction coefficient.

Stanton number – Flat Plate – M=5
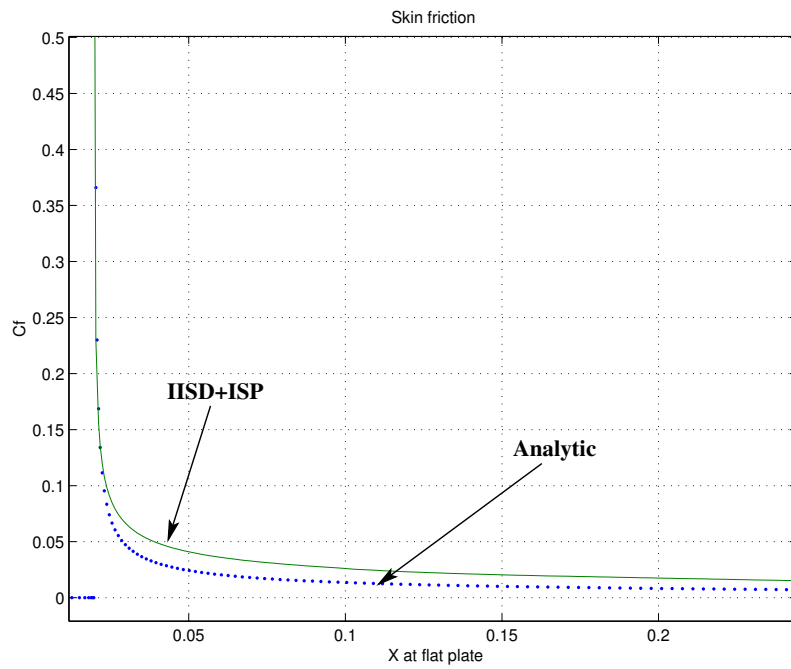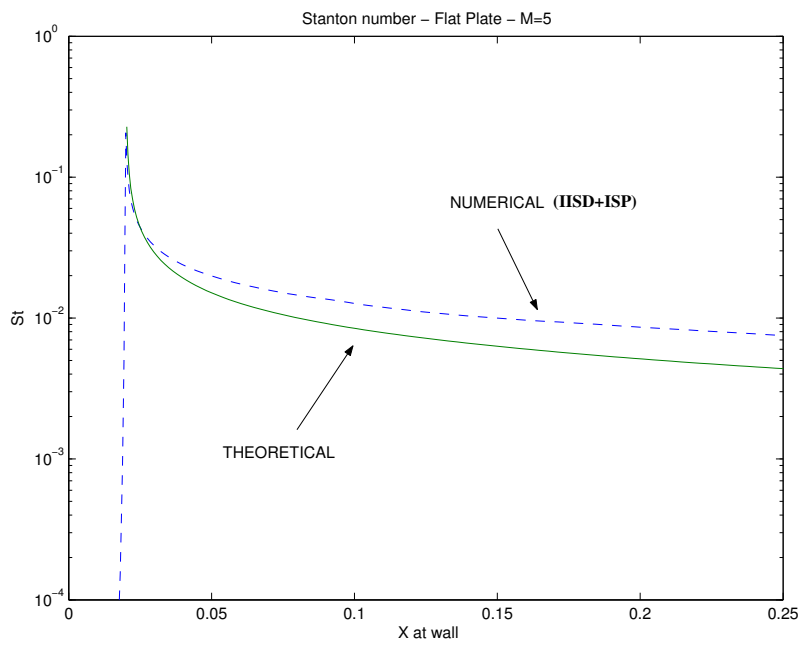
(b) Stanton number.

Figure 2: IISD+ISP solution vs. Theoretical approach.

Table 1: comparison between the analytical reference results and the computed results

	Press. ratio	Temp. ratio	Mach after the shock	Angle of the shock
Present Result	13.482	3.166	5.305	20.37°
Theoretical	13.404	3.194	5.279	19.941°
Relative error	0.6%	0.9%	0.5%	2.1%

invariants are known for Euler equations and the conditions are satified in the nonlinear form.

The table (1) shows the results comparing to the analytical values.

A mesh of 23625 quadrangular elements and 23086 nodes was used. A basic structured mesh was adaptively refined. The basic mesh had a variable step size towards the wall in the vertical direction and towards the corner and leading edge in the horizontal direction. The final mesh had an element at the wall with a size of 1.5×10^{-6} in the normal direction and 1.3×10^{-5} in the tangential direction. In order to perform this test case we used a Q1/Q1 element for the space discretization which means that the velocity, the density and the temperature field are discretized in the same way with linear interpolation. In order to reach the steady state we iterated in time with a backward Euler scheme using 3 Newton-Raphson iterations per time step. The Stanton number was computed estimating the normal derivative of temperature at the wall with a second order finite difference approximation.

Another important point to study is the capacity of the code to simulate the shock without non-physical oscillation. We then analyze the profile of the pressure field along an horizontal cut at the position y = 0.2 (figure (3)).
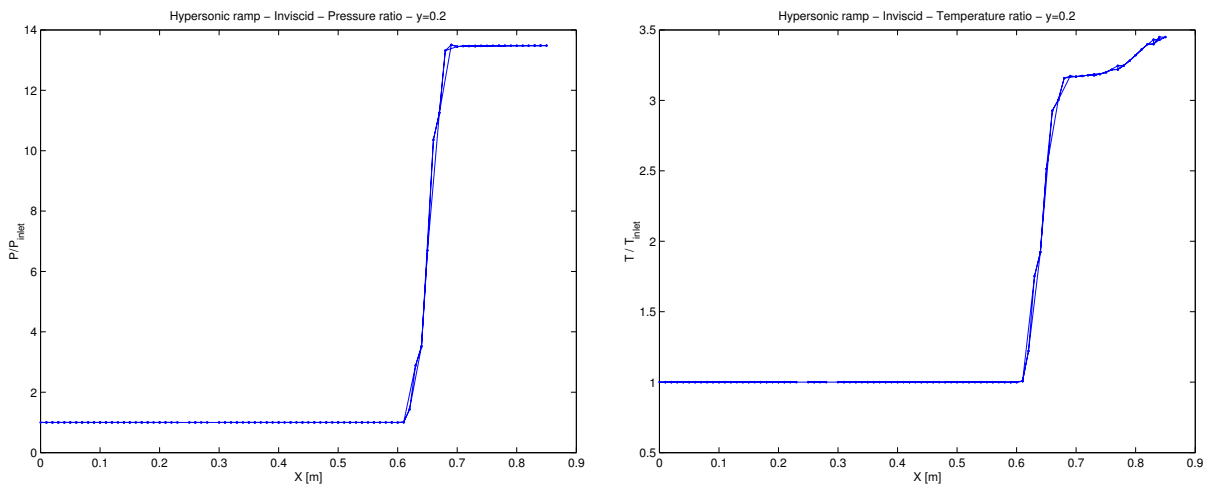
(a) Pres. through the shock wave

(b) Temp. through the shock wave

Figure 3: Results in non-refined grid.

We have to point out that for a y=const cut, we plot values for nodes that fall in a thin strip of nodes around the y value. This is the reason why there seems to be two curves in the cut.

Previous results, obtained on a grid without adaptive refinement, are in general very good but we have observed some problems in the temperature field. Also, on figure (3), we observe that the temperature after the shock continues to increase instead of being constant.

This problem is generated by lack of refinement near the corner. If the corner is not well resolved, then the values behind the shock, near the corner, are different and this is propagated through the streamlines (in this case parallel to the ramp) to a narrow strip near the ramp. This effect can be solved by using adaptive refinement. The temperature ratio field (over the whole domain) with the new adapted mesh can be shown in figure (4).
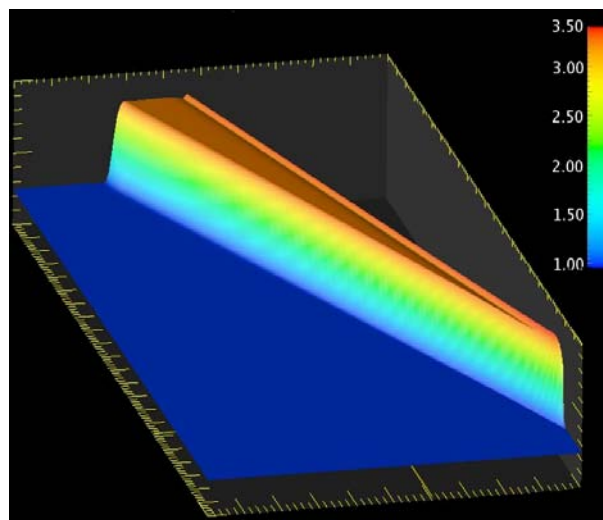
Figure 4: Temperature ratio on the second mesh.

3.3   Viscous hypersonic ramp at Mach=5.

The test case is the isothermal compression ramp at Mach 5. Experimental data are available for the wall pressure coefficient and the wall Stanton number.

The compression ramp is $15°$. The corner is located 0.25 m from the leading edge. This length is used to define the Reynolds number which gives the value 1.5×10^6. The inflow temperature is 80K and the wall temperature is 288K.

The Prandtl number is constant and equals to 0.72. The viscosity is a function of temperature according to Sutherland's law. To conserve attached shock at the corner of the compression ramp, the Mach number at inlet will be chosen equal to 5. The complete characteristics of the inflow are: inlet pressure $p_\infty = 10^5$Pa, gas constant $R = 287$J/(kgK), gas specific heat ratio $\gamma = 1.4$, inlet temperature : 80K and wall temperature $T_{wall} = 288$K. With these values we obtain a speed of sound value of $c = 179.3$m/sec. As initial flow field, we will consider inviscid uniform flow with $M = 5$, $p = 10^5$Pa and $T = 80$K.

3.3.1 Physics of a shock wave/boundary layer interaction.

For two-dimensional shock wave/boundary layer interactions typical of laminar flows over compression ramps with sharp leading edge the physics is rather well understood when unsteady effects are negligible. Referring to figure (5), a relatively weak shock forms at the sharp leading edge of the plate, the shock induced by the ramp interacts with the boundary layer and, due to the upstream propagation of pressure disturbances across the subsonic portion of the boundary layer (i.e. the upstream influence), flow separation may occur depending upon the Mach number, the Reynolds number, the ramp angle, the wall temperature, the strength of the adverse pressure gradient and the boundary layer stability. The presence of the separation bubble causes a deviation of the streamlines and the consequent formation of the separation shock, followed by a nearly constant pressure region (i.e. the plateau) in correspondence with the recirculation. In the separated region the skin-friction is negative and in laminar flows the heat transfer reaches a minimum due to the greater boundary layer thickness that lowers temperature gradients. The recirculation bubble ends with flow reattachment on the ramp surface across the strong reattachment shock. The interaction between separation and reattachment shocks generates a transmitted shock, a shear layer and, depending upon the Mach number, either a shock wave or an expansion fan that interacts with the boundary layer on the ramp. The skin friction and heat transfer rapidly increase downstream of reattachment due to the flow re-compression, and have a peak past reattachment at the location where boundary layer thickness is minimum, then they decrease due to boundary layer thickening (and flow re-acceleration) on the ramp. When analyzing shock wave/boundary layer interaction flows the occurrence of incipient separation and Görtler instabilities past flow reattachment on the ramp must be checked, since both physical features considerably affect the flow field development.

3.3.2 Numerical simulation conducted in a parallel environment.

On the figure (6), we compare the pressure coefficient along the isothermal wall using the Sutherland law with experimental data.

We observe that the general shape of the pressure coefficient along the wall is good. There are oscillations between $x = 0$ and $x = 0.25$ but we observe that the position of the shock is well reproduced according to the experimental data. After the shock, the pressure coefficient is under evaluated.

Concerning the Stanton number, the following results (figure (7)) are obtained from the simulation.

We clearly observe that the Stanton number along the isothermal wall presents important fluctuations between $x=0.225$ and $x=0.25$ which is the corner of the ramp. We also observe that before the corner, the Stanton number is over evaluated and after the corner under evaluated.

In order to explain the fluctuation at the corner of the ramp, we have to analyze to recirculation bubble in the flow. As shown, we clearly see that the proposed grid is not enough fine to capture correctly the recirculation bubble, which cause important problem for the evaluation of the heat transfer. On the figure (8), we observe in red the region where the x-velocity is negative
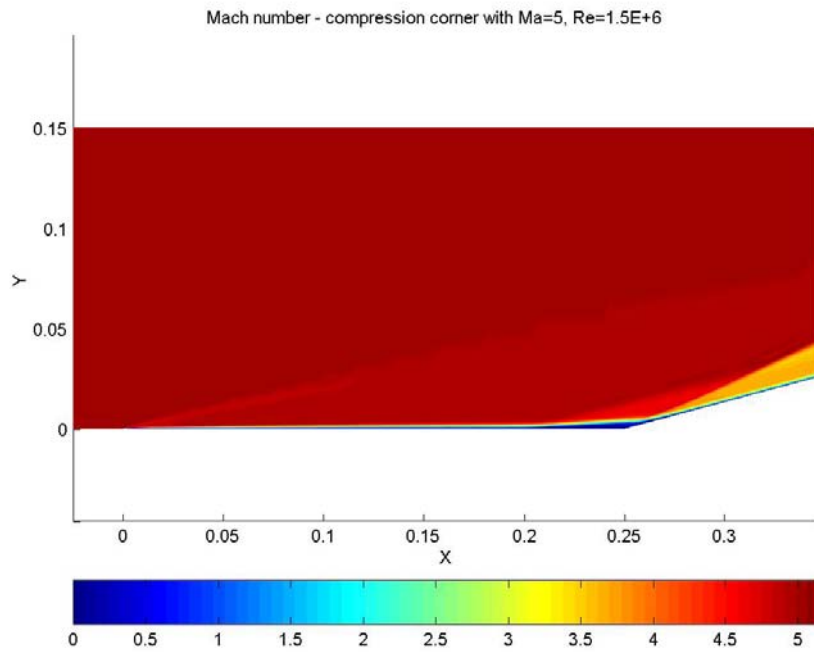
Figure 5: Mach number.
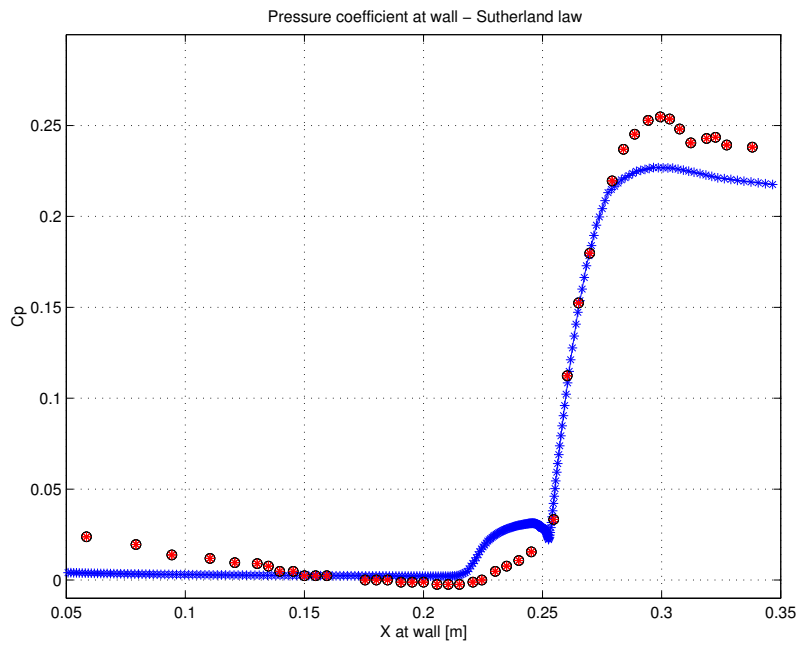
Figure 6: Pressure coefficient along the isothermal wall. In **red**: PETSc-FEM results, **blue**: experimental.
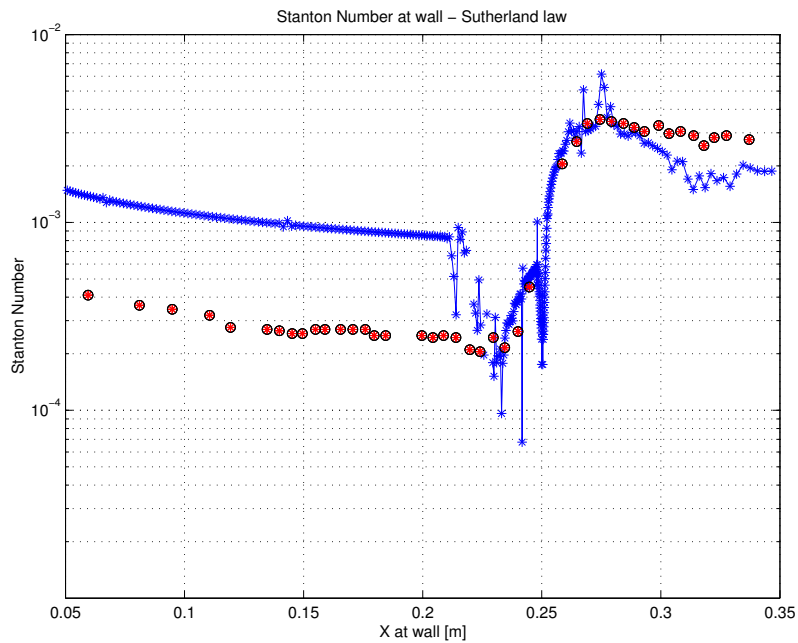
Figure 7: Stanton number along the isothermal wall. In **red**: PETSc-FEM results, **blue**: experimental.

and in blue the regions where the x-velocity is positive. We see one big recirculation zone in red but near the isothermal wall, before the corner, we also observe two small recirculation zone in blue. The presence of such zones shows that the grid is not fine enough to correctly characterize the flow and in particular the heat transfer at the wall.
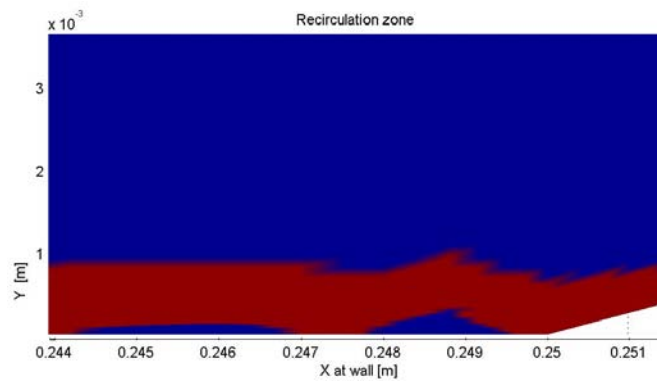
Figure 8: Recirculation zone for the first computation with constant viscosity.

The new distributions of Mach number, Stanton number and skin-friction coefficient are reported in figures (5), (9) and (10), respectively, where a new adapted mesh with the same number of nodes was used.

Figure (12) indicates that the predicted plateau pressure is slightly lower than the measured
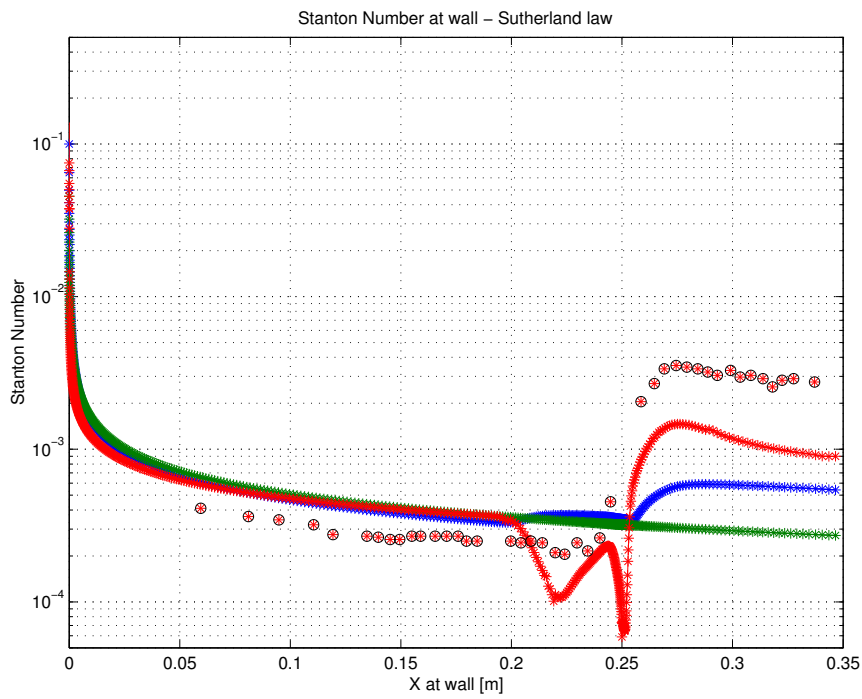
Figure 9: Stanton number (refined mesh). In **red**: PETSc-FEM results, **green**: Blasius analytical approximation, **blue**: Eckert analytical approximation, **circles&stars**: experimental.
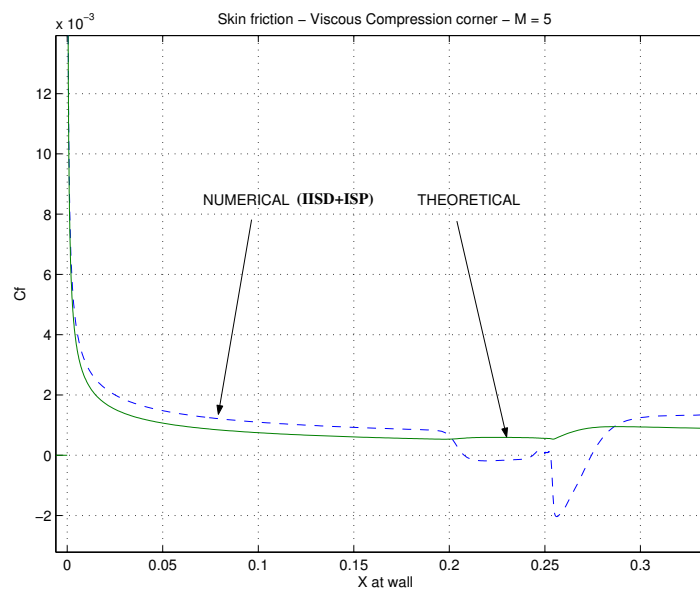
Figure 10: Skin friction coefficient (refined mesh).

one, and the pressure peak is slightly over-predicted, while the computed flow expansion on the ramp is weaker than that evidenced by experiments. Comparison of Stanton number shows a very good agreement with experiments along the entire model, except for a small over-prediction of peak heating. The skin-friction (figure (9)) is well predicted upstream of the interaction (the theoretical distribution given by Eckert's reference enthalpy method is also plotted for comparison). In figures (11) to (13) we can see $x =$ constant cuts for Mach, u/c and p/p_∞. The cuts are at 11 equidistant vertical lines starting at $x = 0.15$ and ending at the corner $x = 0.25$ with intervals of 0.1. The colors identify the section, starting from $x=0.15$ to 0.25.
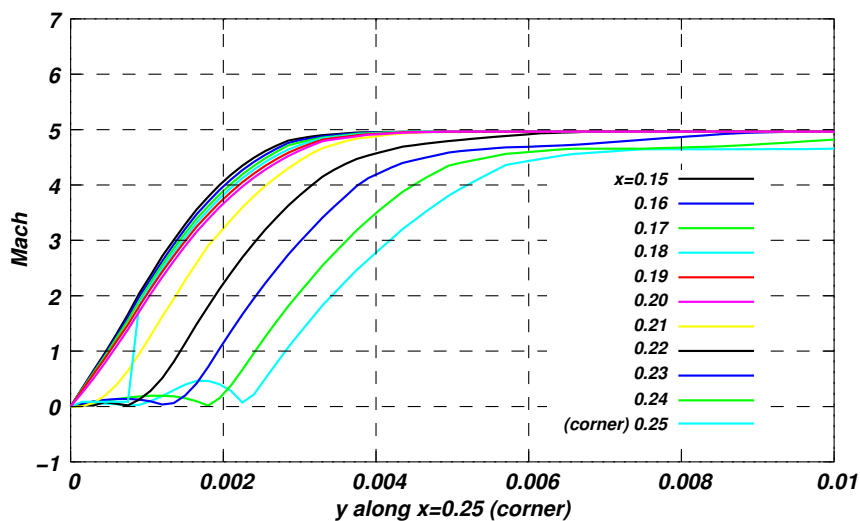
Figure 11: Mach at several $x =$ const cuts, detail near wall.

3.3.3   Efficiency notes.

The mesh has 30032 nodes (120128 degrees of freedom) and 28854 quadrangular elements. Bilinear (Q1) interpolation was used. Adaptive refinement is used for obtaining a grid with a significant refinement towards the wall. The startup time (reading the mesh, graph partitioning and building matrix profiles) is negligible, so that the CPU time can be accurately computed as the time of one time step times the number of time steps. The number of time steps needed to converge can be estimated as 1500. (With the time step used, this number of time steps is enough for a particle to travel 3 times the length of the computational domain.)

In a cluster of Intel Pentium 4, 2.80GHz-HT (1024Kb cache, 2GB RAM) processors we have the following CPU time per time steps.

- For 1 processor: 120.4 secs per time step.
- For 4 processor: 33.6 secs per time step. (Speed-up 3.58, efficiency 89.6%).
- For 10 processors: 18.6 secs per time step. (Speed-up 6.38, efficiency 63.8%).
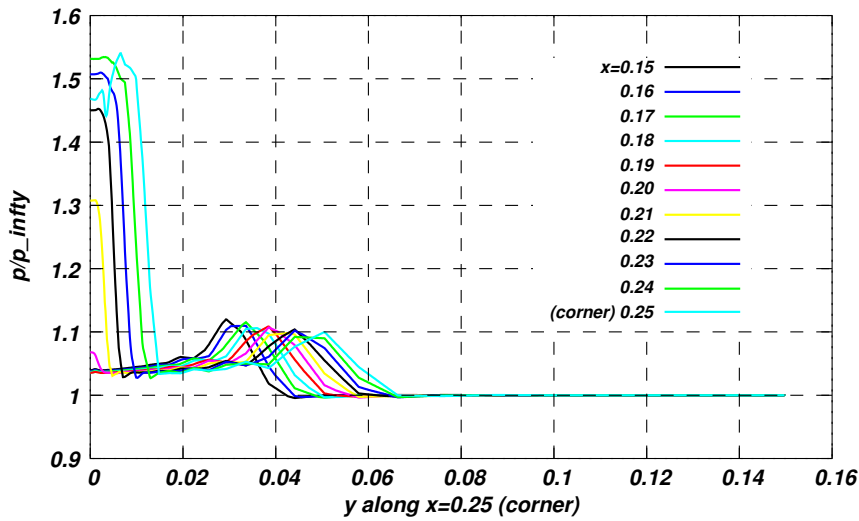
Figure 12: Relative pressure (p/p_∞) at several x =const cuts.
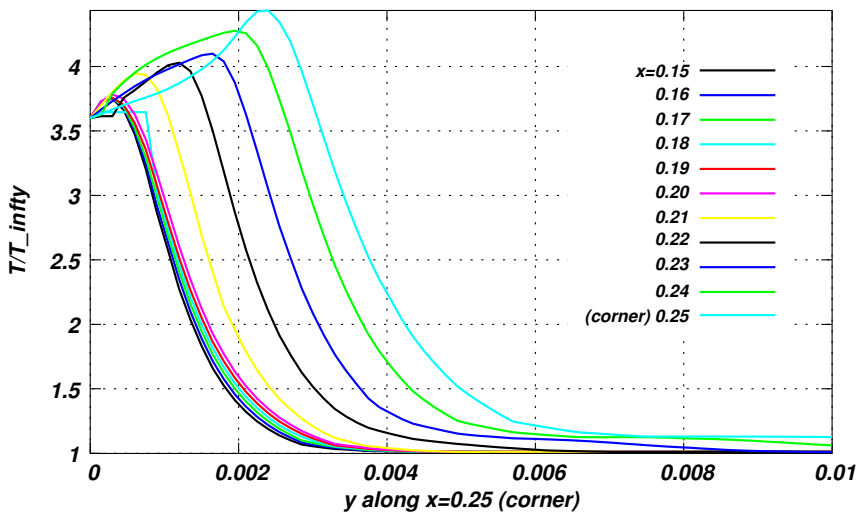
Figure 13: Relative temperature (T/T_∞) at several x =const cuts, detail near wall.

So that, the total computing time ranges from 50 hrs in sequential mode (1 processor) to 7.75 hrs in parallel (10 processors). We used two Newton iterations per time step, so that the CPU time per Newton iteration is one half the CPU time per time step, in general 40% of the CPU time is spent in building the residual and matrices and the rest in solving the linear system with the Domain Decomposition Method and the Interface Strip Preconditioner.

3.4   Shock wave propagation in a Nozzle.

The third test case proposed is the study of the propagation of a shock wave in a nozzle. Even if in a real configuration, the problem has to be 3D, we will consider a 2D geometry of the

nozzle. The contour of the nozzle has been provided by ESA. The test consists in studying the propagation of the shock wave when a brutal rupture of the diaphragm at the inlet occurs until the steady-state problem. Two different time integration schemes were used: a first order temporal scheme and a second order temporal scheme. The fluid is initially at rest and at a pressure of 143Pa, temperature 262K. At time $t = 0$ a membrane at the throat (AD) is broken. Behind the membrane there is a reservoir at 6bar, 4170K. The gas constant is $\gamma = 1.17$. The axial symmetry of the problem is exploited by taking a slice of elements between two meridian planes that cut the z-axis (see figure (14)).
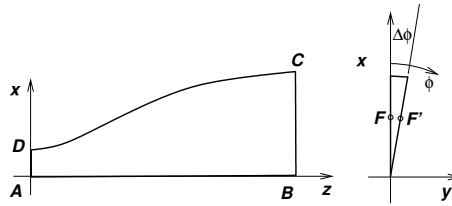
Figure 14: Geometrical description of the problem.

A 3D mesh of hexahedral elements is generated by *"extrusion"* of a quadrangular mesh in the $x - z$ plane in the circumferential direction. Quadrangular elements that have a side on the z-axis generate a *"wedge"* element, i.e. an hexahedra element with a face collapsed in a edge. Periodic boundary conditions are considered between the two meridian planes, i.e. values at a node F' on plane $\phi = \Delta\phi$ is taken from the value of the corresponding node at plane $\phi = 0$ ($x - z$ plane). Scalars are simply copied and vectors are appropriately rotated. The periodic boundary condition reduces on the z axis to $u = v = 0$ and w free. This is, thus, the condition on the z axis. Slip boundary condition is imposed at the wall DC. p, ρ and u, v are imposed at inlet AD, whereas w (axial velocity) is left free. At outlet (BC), an absorbing boundary condition that we called *"ulsar"*[4] is imposed. This guarantees that the proper number of boundary conditions is imposed, since the flow there passes through a number of conditions, from rest to subsonic and supersonic outlet, varying the number of incoming characteristics.

3.4.1 First order temporal scheme.

A first order temporal scheme (backward Euler), with a time step of $\Delta t = 5.143 \times 10^{-6}$ was employed. The propagation of the shock wave is shown in figure (15).

The first curve is for the fifth time step ($t = 5\Delta t = 2.5717 \times 10^{-5}$sec). The second curve is for the 50-th time step ($t = 50\Delta t = 2.5717 \times 10^{-4}$sec). Subsequent curves are plotted each 50 time steps, so that there is a time difference of $50\Delta t = 2.5717 \times 10^{-4}$sec between each curve. The last curve before all the perturbation exits at the outlet is for $t = 7.2 \times 10^{-4}$sec.

The value of the mean velocity of the shock wave (using the previous figure) is 2465.8 m/s and agrees with the measure data (2600-2700 m/s).

After the shock wave has reached the outlet, the steady state is quite rapidly obtained. The Mach number along the z-axis at steady state starts from $M = 1$ at the inlet, according to the
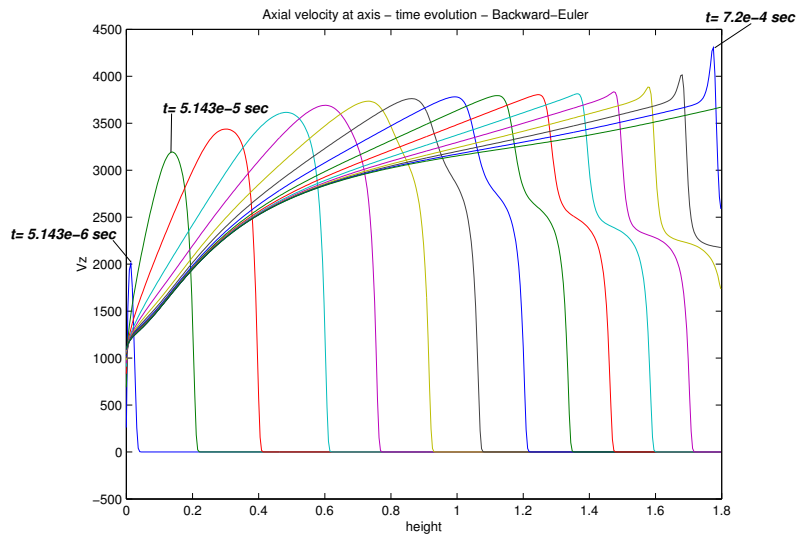
Figure 15: Time evolution of axial velocity (v_z) at z-axis.

theory, and goes up to 3.8 at the outlet as shown on the figure (16) (this plot corresponds to the second order scheme simulation, but there is no substantial differences with the first order scheme results).

Enthalpy and mass Conservation: In the steady state we checked for mass and enthalpy conservation by integrating the mass (ρw) and enthalpy ($\rho h w$) flow in the inlet and outlet planes using the standard FEM interpolation. The mass flow is $6.2860 \mathrm{Kg/sec}$ at inlet and $6.2871 \mathrm{Kg/sec}$ at outlet (relative error is 2.5×10^{-4}), whereas the enthalpy flow is $5.8753 \times 10^7 \mathrm{Kg\,m^2/sec^3}$ at inlet $5.9690 \times 10^7 \mathrm{Kg\,m^2/sec^3}$ at outlet (relative error of 1.1×10^{-3}).

3.4.2 Second order temporal scheme.

A second simulation were performed for this test case using a second order temporal scheme. The temporal scheme is now the Crank-Nicolson scheme, which has second order temporal accuracy. Using this second order temporal scheme, we obtain the time evolution of the axial velocity at z-axis which yields a shock velocity of 2620.5 m/s.

On the physical wall of the domain, the Mach distribution is slightly different from the one obtained along the z-axis. The Mach number becomes high quickly and in a monotone way (see figure (16).

Enthalpy and mass Conservation: With this temporal scheme the mass flow is $6.2542 \mathrm{Kg/sec}$ at inlet and $6.2680 \mathrm{Kg/sec}$ at outlet (relative error is 2.17×10^{-3}), whereas the enthalpy flow is $5.8545 \times 10^7 \mathrm{Kg\,m^2/sec^3}$ at inlet and $6.8369 \times 10^7 \mathrm{Kg\,m^2/sec^3}$ at outlet (relative error 3×10^{-3}).

The CFL number was computed as $\mathrm{CFL} = (|\mathbf{u}| + c)\Delta t/h$. h was taken constant as the mesh step size in the axial direction, i.e. $h = 4.4938 \times 10^{-3}$. A colormap of the CFL number is shown at figure (17). The maximum CFL is near the shock and reaches 1.4.
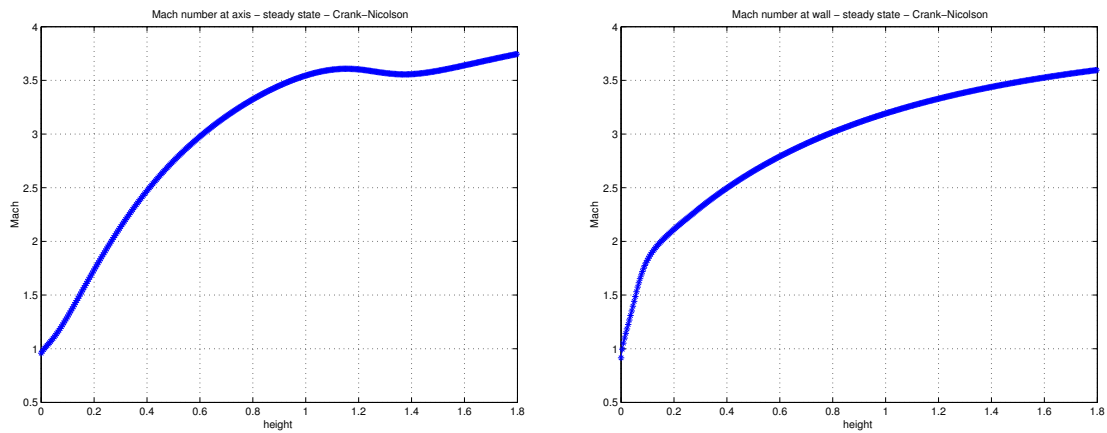
Figure 16: Mach number: along the z-axis (**left**); at the wall DC (**right**)
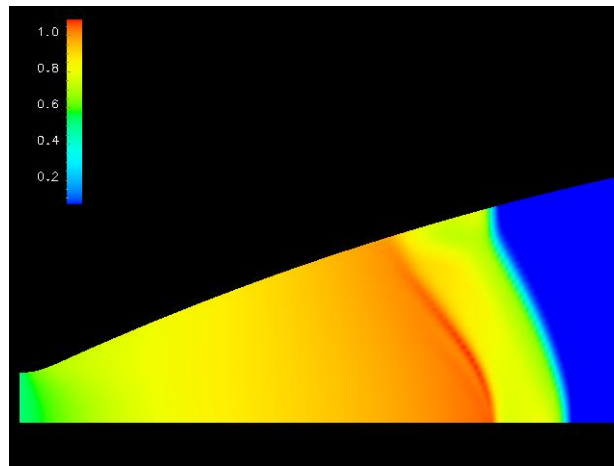
Figure 17: Colormap for CFL= $(|\mathbf{u}| + c)\Delta t/h$.

3.4.3   Computing time for the nozzle.

The mesh has 24892 nodes, (124460 degrees of freedom), 12000 hexahedral elements (bilinear Q1 interpolation).

   In a cluster of Intel Pentium 4, 2.80GHz-HT (1024Kb cache, 2GB RAM) processors we have the following CPU time per time steps (3 Newton iterations per time step).

- For 1 processor: 62.5 secs per Newton iteration, 187.5 secs/time step.
- For 4 processors: 17.83 secs per Newton iteration, 53.5 secs/time step (speed-up 3.5, efficiency 87%).
- For 10 processors: 9.83 secs per Newton iteration, 29.5 secs/time step (speed-up 6.4, efficiency 64%).

The number of time steps until the flow reaches the steady state can be estimated as 900, so
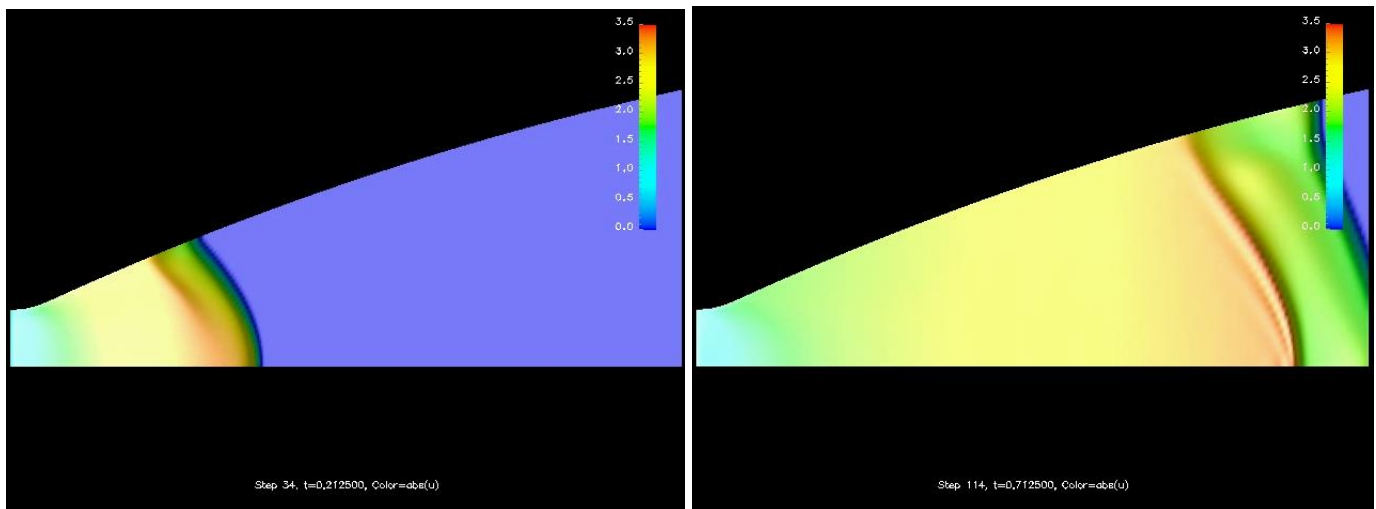
Figure 18: $||\mathbf{u}||$ in two different time steps.

that the total computing time ranges from 47 hrs in sequential mode (1 processor) to 7.37 hrs in parallel (10 processors).

Note on parallel efficiency: It must be taken into account that the size of the problem is too small to give high efficiency for 10 processors in both examples. Higher efficiencies are obtained for a larger problem.

4 CONCLUSIONS AND FUTURE WORK.

In this work a variety of challenge problems involving viscous/inviscid compressible flows at hypersonic Mach number were considered. This paper emphasizes on the quality and the efficiency of solver schemes for CFD problems. Both criteria should be evaluated together to analyze the performance of a simulation. Reasonable efficiency might not be very significant if the solution is not accurate enough for the final purpose. Numerical experiments of several physical (real) problems have been carried out to show its computation time and memory requirements using monolithic schemes. Through these tests, it was shown that it is not always possible to obtain an acceptable solution for the problem using classical global Krylov methods (like preconditioned global GMRes one). Domain Decomposition techniques, especially the Schur Complement Domain Decomposition using the Interface Strip Preconditioner, are suitable in order to achieve accurate solutions efficiently. The IS preconditioner is well suited for flows with high Mach numbers and high Reynolds numbers where the contribution of advective terms are predominant in the governing equations. Furthermore, IISD+ISP is a good alternative to treat problems where domain discretization presents high refinement gradients.

Future work will consider chemical reactions to correct the prediction of the heat conduction and the imposition of conditions to simulate radiation effects in a wide wavelength range of the spectra. Also, in a major state of the code, a *strong interaction* of this kind of flow with structural components will be treated.

ACKNOWLEDGMENTS

REFERENCES

[1] MA Storti, L. Dalcin, RR. Paz, A. Yommi, V. Sonzogni, and NM. Nigro. An interface strip preconditioner for domain decomposition methods. to appear in. *Journal of Computer Methods in Science and Engineering*, (2003). in press.

[2] RR. Paz and MA. Storti. An interface strip preconditioner for domain decomposition methods: Application to hydrology. *International Journal for Numerical Methods in Engineering*, **62(13)**, 1873–1894 (2005).

[3] RR. Paz, NM. Nigro, and MA. Storti. On the efficiency and quality of numerical solutions in cfd problems using the interface strip preconditioner for domain decomposition methods. *International Journal for Numerical Methods in Fluids*, (2005). submitted.

[4] MA. Storti, NM. Nigro, RR. Paz, and LD. Dalcín. Dynamic boundary conditions in fluid mechanics. In *VIII Congreso Argentino de Mecnica Computacional. MECOM 2005*, (2005). submitted.

[5] DR. Chapman, DM. Kuehn, and HK. Larson. Investigation of separated flows in supersonic and subsonic streams with emphasis on the effect of transition. *NACA-TN3869, NACA Rep. 1356.*, (1957).

[6] JM. Délery. Shock interference phenomena in hypersonic flows. In *The Third Joint Europe/US Short Course in Hypersonics.*, (1990).

[7] MS. Holden. Two-dimensional shock wave-boundary layer interactions in high speed flows. part ii, experimental studies on shock wave-boundary layer interactions. *AGARDograph AG-203*, pages 41–110 (1975).

[8] GA. Sod. A survey of several finite difference methods for systems of nonlinear hyperbolic conservation laws. *Journal of Computational Physics*, **27**, 1–31 (1978).

[9] G. Moretti. A fast euler solver for steady flows. *AIAA Paper, Proc. AIAA 6th Computational Fluid Dynamics Conference*, **83-1940**, 357–362 (1983).

[10] C. Hirsch, C. Lacor, and H. Decorninck. Convection algortithms based on a diagonalization procedure for the multidimensional euler equations. *AIAA Paper, Proc. AIAA 8th Computational Fluid Dynamics Conference*, **87-1163**, 667–676 (1987).

[11] F. Grasso and M. Marini. Multigrid techniques for hypersonic viscous flows. *AIAA Paper*, **93-0771** (1993).

[12] F. Grasso and M. Marini. Tvd multigrid solutions of three dimensional viscous hypersonic

flow. *AIAA Paper*, **950470** (1995).

[13] L. Jiang, CL. Chang, M. Choudhari, and C. Liu. Instability-wave propagation in boundary-layer flows at subsonic through hypersonic mach numbers. *Mathematics and Computers in Simulation*, **65**, 469–487 (2004).

[14] X. Zhong and M. Tatineni. High-order non-uniform grid schemes for numerical simulation of hypersonic boundary-layer stability and transition. *Journal of Computational Physics*, **190**, 419–458 (2003).

[15] W. Rachowicz. An anisotropic h-adaptive finite element method for compressible navier-stokes equations. *Computer Methods in Applied Mechanics and Engineering*, **146**, 231–252 (1997).

[16] AN. Brooks and TJR. Hughes. Streamline upwind/petrov-galerkin formulations for convection dominated flows with particular emphasis on the incompressible navier-stokes equations. *Computer Methods in Applied Mechanics and Engineering*, **32**, 199–259 (1982).

[17] S. Aliabadi, S. Ray, and T. Tezduyar. Supg finite element computation of viscous compressible flows based on the conservation and entropy variables formulations. *Computational Mechanics*, **11**, 300–312 (1993).

[18] T. Tezduyar, S. Mittal, S. Ray, and R. Shih. Incompressible flow computations with stabilized bilinear and linear equal order interpolation velocity pressure elements. *Computer Methods in Applied Mechanics and Engineering*, **95(95)**, 221–242 (1992).

[19] T. Tezduyar and M. Senga. Determination of the shock-capturing parameters in supg formulation of compressible flows. In Tsinghua University Press & Springler-Verlag, editor, *Computational Mechanics WCCM IV, Beijing, China 2004.*, (2004).

[20] G. Rios Rodriguez, E. López, M. Nigro, and M. Storti. Refinamiento adaptativo homogeneo de mallas aplicable a problemas bi y tridimensionales. In *VIII Congreso Argentino de Mecnica Computacional. MECOM 2005*, (2005). submitted.

[21] R. R. Paz, M. A. Storti, S. R. Idelsohn, L. B. Rodríguez, and C. Vionnet. Parallel finite element model for coupled surface and subsurface flow in hydrology: Province of santa fe basin, absorbent boundary condition. In *XIII Argentine Congress on Computational Mechanics - ENIEF2003*, (2003).

[22] MA. Storti, NM. Nigro, and RR. Paz. PETSc-FEM: A general purpose, parallel, multi-physics fem program. (1999-2005).

[23] JE. Carter. Numerical solutions of the navier-stokes equations for the supersonic laminar flow over two-dimensional compression corner. *National Aeronautics ans Space Administration (NASA), Thechnical Report R-385*, (1972).

[24] F. Grasso, G. Leone, and J. Délery. Validation procedure for the analysis of shock-wave/boundary-layer interaction problems. *AIAA Journal*, **32(9)**, 1820–1827 (1992).